1-1-2010

Monitoring vascular changes induced by photodynamic therapy using contrast-enhanced micro-computed tomography

Otilia Cristina Nasui
Ryerson University

MONITORING VASCULAR CHANGES INDUCED BY PHOTODYNAMIC THERAPY USING CONTRAST-ENHANCED MICRO-COMPUTED TOMOGRAPHY

by

Otilia Cristina Nasui

B.Sc., University of Toronto, Toronto (2007)
B.Ed., Queen's University, Kingston (2008)

A thesis submitted in conformity with the requirements
for the degree of Master of Science
in the program of Biomedical Physics
Ryerson University

Author's declaration

I hereby declare that I am the sole author of this thesis. I authorize Ryerson University to lend this thesis to other institutions or individuals for the purpose of scholarly research.

_____

I further authorize Ryerson University to reproduce this thesis by photocopying or by other means, in total or in part, at the request of other institutions or individuals for the purpose of scholarly research.

_____

MONITORING VASCULAR CHANGES INDUCED BY PHOTODYNAMIC THERAPY USING CONTRAST-ENHANCED MICRO-COMPUTED TOMOGRAPHY

Otilia Cristina Nasui, M.Sc. in Biomedical Physics
Ryerson University, Toronto (2010)

Abstract

The aim of this study is to determine if contrast-enhanced micro-computed tomography can be used to non-invasively image the response of vasculature in tumours that have been treated with photodynamic therapy (PDT). The subjects used were C3H mice with RIF-1 tumour implanted subcutaneously and allowed to grow for 3 weeks prior to treatment. The subjects in this study were divided into PDT treated groups (150 J/cm^2, 50 J/cm^2) and control groups (150 J/cm^2 light-only, untreated). The contrast-enhanced micro-computed tomography imaging procedure consisted of eight-second scans taking place before treatment and up to 24 hours after treatment. The treatment response was evaluated through the ratio of blood-to-tumour volume. Significant changes were detected at 8 and 24 hours in the 150 J/cm^2 PDT group ($p < 0.01$). Immunohistochemical staining confirmed the effects of each treatment in comparison to the control groups.

Acknowledgements

I would like to send my gratitude to my thesis supervisor Prof. N. Ford for her guidance and support through this thesis. I would also like to thank Dr. S. Bisland, Prof. R. Karshafian and Prof. M. Kolios for all the helpful questions posed in meetings and occasional thesis-related discussions.

I would like to acknowledge Dr. B. Wilson at Princess Margaret Hospital in Toronto for sharing his equipment for the photodynamic therapy side of the experiment at the base of this thesis.

Dedicated to my parents, Mioara and Ilie, for all the advice they had to offer along the way.

A special dedication goes out to Jesse for his constant love and support.

Contents

List of Tables

List of Figures

Chapter 1

Introduction

1.1 Photodynamic therapy

Photodynamic therapy (PDT) is a type of treatment used to eradicate diseased tissue. A photosensitizer is administered and it distributes selectively at the tumour site while remaining inactive. Then light of a specific wavelength is used to irradiate the tissue and induce tumour destruction. This allows for selective destruction of tumours while avoiding damage to adjacent healthy tissue. Depending on the photosensitizer used, the effects induced can be cellular or vascular. The treatment is completed by activating the photosensitizer through the use of focused light of a specific wavelength compatible with the photosensitizer used.

PDT mechanism. Each photosensitizer activation is a function of laser wavelength. The energy deposition by light irradiation triggers a release of oxygen molecules in their singlet state at the cellular level. This is a highly toxic species of oxygen with an area of action of about 0.02 μm [1]. So structures at a distance farther than 0.02 μm from the starting point of the cytotoxic reaction will not be affected.

Photosensitizers. The effects of photosensitizers can be vascular and non-vascular, depending on the time interval between the photosensitizer injection and tissue ir-

radiation. Different photosensitizers vary in the time they take to leak out of the blood vessels and into the surrounding tissues. Therefore the time of irradiation determines the nature of the PDT effect. A photosensitizer located in the blood vessels at the time of irradiation promotes endothelial collapse as the first step in PDT [2]. Some of the newer techniques look at fractionation of PDT (*ie.* segmenting the delivery of light) with good results in overcoming oxygen limitations in the tissues treated [3]. These limitations refer to fixed amounts of oxygen available in the tissue. If PDT is successful, it is because the oxygen in the region is used for the cytotoxic reaction causing cell or epithelial damage. Even if the photosensitizer is still available and the tissue continues to be irradiated, there is no longer a cytotoxic effect to PDT once the tissue oxygen level drops. Hence the effect of PDT is maximized by distributing the light dose evenly at time-points when the oxygen levels in the region have been restored.

Benzoporphyrin derivative monoacid ring (BPD-MA) has been previously shown to induce vascular collapse in eye conditions and tumours [4]. The preference in this study for this particular photosensitizer was guided by previously published studies showing that for 15- to 30-minute intervals between photosensitizer administration and light irradiation are preferable over 3-hour intervals if vasculature is the PDT target. According to other study reports, after 30 minutes, the photosensitizer leaks out of the vasculature and into the surrounding tissue [5, 6, 7, 8] making the vascular PDT less effective.

Light irradiation. The properties of the laser beam and the optical properties of the tissue are also important in the treatment response. The depth of penetration of light into the tissue determines the depth of PDT. Light intensity decreases exponentially as it travels through tissue, so the adjacent tissue is not affected by PDT [9, 10]. Experimentally it has been determined that each photosensitizer requires a specific wavelength of laser beam activation. In the case of BPD-MA, some studies have been done using 630 nm [11, 12, 3] or 650 nm [13] instead of the typical 690 nm but with fairly similar results. Finally, the power of the activation

beam delivered also affects the PDT response. It has been noted that using a low power setting (below 200 mW/cm^2 [9]) avoids potential interference of PDT and thermal effects in the tissue.

1.2 Motivation

1.2.1 Current clinical applications of photodynamic therapy

The current method used clinically for monitoring the effects of the treatment is biopsy. This is an invasive technique, uncomfortable for the patient and unable to give a full picture of treatment effects - neither spatially nor temporally. Spatially, small volumes of tissue from within the tumour are sampled through the use of a needle. This sampled tissue is then analyzed for specific biological markers and a diagnostic is given for the result of the treatment. But an evaluation of the entire treated volume is not possible. Biopsies are taken at one point in time and so the results do not reflect any progress of the effects of PDT. Sometimes biopsies are repeated if suspicions about the progress are made but at large intervals of time. Overall, biopsies are not an adequate tool to monitor the evolution of the treatment in time due to its invasive nature.

False negatives are known to be frequent with biopsies and the effects of the treatment also differ from patient to patient in terms of time-scale or degree of effects; hence, patients often get called back for repeated biopsies. Although the treatment method is minimally invasive, in order to monitor the effects properly, biopsies need to be performed and sometimes repeated. This makes the monitoring of treatment effects more invasive than the treatment itself. Therefore a search for more efficient and less invasive method of monitoring the PDT effects is ongoing. Current research studies focus on developing protocols for imaging systems that can be translated to clinical use for monitoring treatments in the preclinical stage. The main imaging modalities used are optical coherence tomography, ultrasound

and magnetic resonance imaging. These techniques offer good spatial and contrast resolution.

But optical coherence tomography (OCT) and ultrasound suffer from limited penetration depth. While OCT is limited to 1 – 2 mm below the surface, ultrasound quickly deteriorates in lateral resolution as depth of imaging is increased (for specific transducer diameters, lateral resolution is proportional to the depth of beam focus and wavelength of the wave). While ultrasound can be used for imaging at higher depths than OCT, visibility of the imaging structures might not be possible (*ie.* when the size of the image structures is smaller than the lateral resolution, which will occur for deeper penetrations of the ultrasound beam).

More specifically, clinical Doppler ultrasound uses 1-12 MHz signals to measure vascular function. Frequencies of above 20 MHz have been used for improved assessment of blood flow at depths of 5-10 mm with lateral resolutions of 50-150 μm [14]. In the case of OCT [15], within the 1-2 mm depth limit, depending on the wavelength, type of laser, power of the source and type of tissue used, the resolution changes drastically. For example, in the case of histological slides, it was possible to distinguish between different layers of the blood vessel when using 1300 ± 72 nm with a source power of 5 mW. But in an *in vivo* scan, other than the depth limitation, motion artifacts would make this type of imaging unproductive.

In magnetic resonance imaging, the duration of scans is a problem in preclinical studies as it becomes difficult to make a sensitive identification of specific time-points, where effects are best monitored. These points highlight the need for a volumetric imaging modality capable of fast scans, while providing good depth penetration along with excellent contrast resolution.

1.3 Physics of contrast-enhanced micro-computed tomography

1.3.1 The basics of computed tomography imaging

Computed tomography is a type of imaging of anatomical structures through the use of x-rays. X-ray photons are generated by means of an anode plate. These photons are in the 20 – 100 keV range for diagnostic purposes. They can be filtered to create a close-to monoenergetic profile beam. In most cases however, photons arrive at the target in a spectrum of energies. The beam of photons can be manipulated to form a pencil, fan or cone beam on its way to the subject. Once arriving at the subject they penetrate the subject of study following mechanisms of attenuation described below.

Attenuation of x-rays in tissue

The x-ray beam travels through the tissue and is attenuated. The amount of attenuation is represented by means of a linear attenuation coefficient μ measured in cm^{-1}. Linear attenuation coefficients for different tissues were established experimentally in the past. From those experimental results, it is known that bone has a much higher μ than soft tissues. This can be noticed in the three-dimensional CT images formed as bone appears to be white while soft tissue are darker.

Beer-Lambert's law, describing the attenuation of x-rays in tissue, relates the intensity of the incident (I_0) and the transmitted (I) beam with the linear attenuation coefficient (μ) and the distance (x) traveled by the x-ray beam through the tissue before reaching the detector, in the following manner:

$$I = I_0 e^{-\mu x} \tag{1.1}$$

The CT number and μ

Each voxel (cubic pixel) in the image displayed after the scan has a grey-scale value corresponding to the attenuation coefficient of the tissue represented by that voxel. This value is called a CT number and it is displayed in Hounsfield units (HU) because CT scanners are calibrated using water as reference.

In order to relate the attenuation of the tissue of interest (μ_{tissue}) to a voxel's CT number, the transformation below is used:

$$CT\ number = 1000 \cdot \frac{\mu_{tissue} - \mu_{water}}{\mu_{water}} \tag{1.2}$$

Therefore, the three-dimensional image provided through CT scans is a map of the attenuation value of incident x-rays at each location in the body that the x-rays passed through.

1.3.2 The contrast of computed tomography images

The quality of the images formed as a result of CT scans is determined in part by the contrast levels displayed. The contrast levels are what allow one to distinguish between different types of tissues. This contrast is the end result of natural or electronic manipulations of beam properties and of electronic information occurring during image acquisition, image processing and image display [16].

The sources of image contrast

Image contrast results from the differences in energy-dependent linear attenuation coefficients of different tissues [17]. As Bushberg mentioned in his book [16], a 20 keV change in beam energy from 40 to 20 keV results in an increase in the contrast ratio between soft tissues and bone for example. While beams of energy of less than 25 keV interact with tissues by means of photoelectric effect ($\mu \propto \mathrm{E}^{-3}$), beams of energy of 30 keV and above interact with tissues through Compton scattering ($\mu \propto \mathrm{E}^{-0.5}$). Therefore the highest contrast will occur at lower energies – the optimal

energy for best contrast has been shown to be 25 keV for a 3 cm-diameter phantom (representative of a mouse) when compared to the profile obtained with a phantom of diameter representative of that of a human body [18]. In the case of spectral CT scanners where an interval of energies (20 – 100 keV [19, 20, 18]) is used and the x-ray beams are not monochromatic, the attenuation coefficient μ is a linear combination of $\mu_{photoelectric}$ and $\mu_{Compton}$ [21, 22, 23].

The nature of the detector also dictates the changes in contrast. The detector contrast is determined by the nature of the conversion of the signal intensity (or of the energy of the transmitted x-ray beam) into an output signal. In the case of solid-state flat-panel detectors, high contrast is maintained independently of the dose delivered into the tissues. First the x-rays incident on the detector are converted to visible light which give rise to an electric charge which is proportional to the energy of the x-ray beam. This charge is stored in a capacitor which is then transferred to a transistor for analog-to-digital conversion of the signal.

Finally, in the image displayed, the contrast is determined interactively. After reconstruction, the image can be displayed using software – either complementary to the scanner or independent that allows re-mapping of image voxel grey-values so that a different contrast level is achieved. This is done to highlight particular physiological structures through increasing the contrast between tissues that would otherwise be indistinguishable due to similar attenuation levels (illustrated in Fig. 1.1). In such an image, it becomes difficult to resolve differences among tissues that would otherwise be possible (using 5000 grey-scale steps for example). A re-mapping described in Eq. 1.3 allows for a display of CT numbers in the perceptible grey-scale range of 512 steps [24].

The parameters that allow this type of re-mapping are called *width* (W) and *level* (L) of the image window. For this type of re-mapping in clinical scanners, the piecewise linear function below is used to create a relationship between grey-scale values and CT numbers [24]:

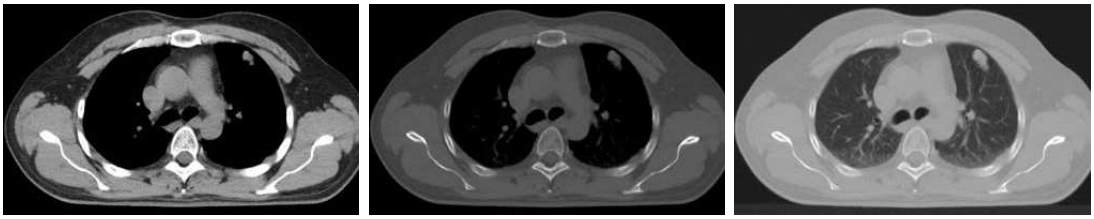

Figure 1.1: Illustration of how different types of CT number mapping changes the contrast between different tissues: Left-hand side (L = 50 HU, W = 350 HU) – soft tissue differentiation; Middle (L = 300 HU, W = 1500 HU) – bone visibility; Right-hand side (L = -200 HU, W = 2000 HU) – lung visibility.

$$grey{-}scale\ value = 511 \cdot \begin{cases} 0, & \text{if CT number} \leq L - \frac{W}{2} \\ \frac{1}{W} \cdot (\text{CT number} - L + \frac{W}{2}), & \text{if CT number} \approx L \\ 1, & \text{if CT number} \geq L + \frac{W}{2} \end{cases} \tag{1.3}$$

Soft tissue contrast in computed tomography

Adjustments in contrast settings in the image display step can make some tissues more visible (as shown in Fig. 1.1 adapted from [24]) depending on the features of interest. However, while the display contrast can be adjusted, the inherent properties of tissues cannot be changed and the subject contrast remains a limitation before and including the step of image display.

The inherent tissue properties affect image contrast. Different soft tissues are known to have similar levels of x-ray attenuation which translates into poor contrast making it difficult to distinguish between different types of soft tissues. Some exemplary values are included in Table 1.1 to illustrate this concept. As mentioned before, attenuation levels, and therefore contrast levels, also depend on the energy of the incident beam [25]. This is why the linear attenuation coefficients in Table 1.1 (adapted from [26]) are specified for the particular beam energies at which they were recorded.

Type of tissue	μ (cm^{-1})	CT number (HU)
Bone	0.528	500+
Blood	0.208	10
Grey matter	0.212	40
White matter	0.213	25
Water	0.206	0
Fat	0.185	-50
Air	0.0004	-1000

Table 1.1: Linear attenuation coefficients for different tissues at 60 keV. Distribution of mean CT numbers of different tissues – on the Hounsfield scale.

1.3.3 Contrast enhancement in computed tomography

In micro-CT, for a given x-ray energy, the contrast level is dominated by the atomic number and concentration of the element that the x-ray passes through on its way to the detector [27]. But the similar linear attenuation coefficients of different soft tissues result in poor contrast between soft tissues in the CT image. It becomes difficult to distinguish between different soft tissues or between blood vessels and the surrounding tissue. The solution is to introduce a contrast agent of a high μ value to act as an opacifying agent in the areas where it localizes. A decrease in intensity of the transmitted beam (I) passing through the contrast agent will occur due to an increased linear attenuation of the x-ray beam in the region occupied by the contrast agent. At the detector, a weaker signal is detected and displayed in the image through a higher CT number. The specificity of contrast agents for certain tissues results in those tissues being picked up as stronger attenuators at the level of the detector. A vascular example of this is illustrated in Fig. 1.2. The picture illustrates a coronal slice from a three-dimensional image of a mouse before and after the administration of a contrast agent within the blood vessels. The femoral artery only becomes visible after the contrast agent's arrival at the site to locally increase the attenuation of the x-rays passing through the femoral artery.

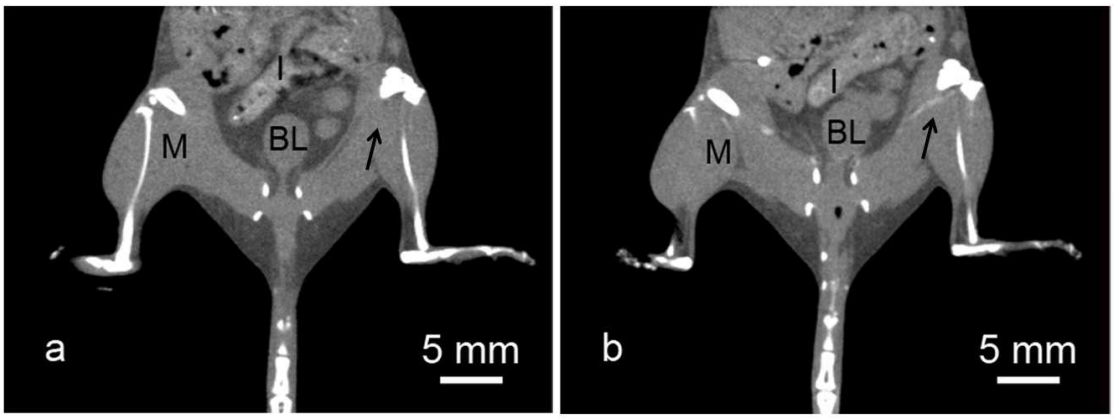

Figure 1.2: A coronal slice of a three-dimensional image of a mouse obtained with a GE Ultra Locus micro-CT scanner using isotropic voxel spacing. The arrow indicates the location of the femoral artery enhanced by the contrast agent administered: a) pre-contrast agent; b) post-contrast agent.

1.3.3.1 Physiological and scanner variables in levels of contrast enhancement

X-ray dose. In an ideal case, lower x-ray energies give higher contrast between the imaged structures. However this method is not practical due to high absorption of low energy photons by the skin. This translates to a small number of low energy photons reaching the deep-seated targeted tissue and even fewer photons reaching the detector. Therefore the image obtained with low energy photons exhibits a high noise level and so the image fails to be useful.

When using a spectrum of higher energy for the incident photons (used for diagnostic purposes) a higher number of photons reaches the detector. This translates to a decrease in the image noise. Therefore, even though the tissue contrast in the image decreases, the contrast-to-noise ratio increases. The downside of this shift in energy is an increase in the x-ray dose delivered to the more deep-seated tissues (unaffected when using low-energy x-rays).

It has been noted that for good contrast without the use of contrast agents one preclinical scan in rodents can be anywhere between 0.17 – 0.80 Gy [28, 29]. The limit to the amount of radiation that can be used for live animal imaging is

given as the lethal dose (LD50/30). LD50/30 is the wholebody radiation dose that would kill 50% of an exposed population within 30 days of exposure. In a mouse, LD50/30 ranges from 5.0 to 7.6 Gy [30, 31, 32, 33] – the variation is a function of the strain of mouse, age at the time of the scan and type of scan (full body or regional).

In the case of studies involving longitudinal scanning, the effects of sublethal radiation doses vary with number of repetitions, frequency of scans and total dose delivered per scan. More specifically, the rate of life shortening in mice has been estimated to be approximately 7.2% per Gy delivered with each whole-body exposure [31]. But, the residual radiation damage can still accumulate up to a deadly level [33]. Although daily doses of 0.25 - 0.5 Gy per day are neutralized, continued radiation exposure damages the recovery process [33]. However in the case of partial body irradiation, the recovery process seems to be more effective (especially when considering lower body irradiation, where the recovery rate is approximately 33% of the LD50/30 per day [32]).

Resolution and biological structure. A combination of physiological and technological factors will affect the contrast in the image displayed.

Firstly, the important physiological factors affecting the final level of contrast agent enhancement are the concentration of contrast agent administered and the body weight of the subject scanned [25]. The contrast enhancement obtained is directly proportional to the concentration injected, for a given body weight [34, 35].

Secondly, there is a dependence of contrast enhancement on two interrelated factors – the size of the structure that is contrast-enhanced and the resolution of the scanning system. This dependence was studied by Plewes [36] and Baxter [37] using phantoms. Plewes concluded that partial volume averaging in CT reduces the contrast of small structures. Baxter further analyzed this issue to find that for objects larger than about one resolution element and aligned with the scanner axis, CT numbers may be determined accurately.

In our study, this translates to the following: if the size of the voxel is smaller

than the contrast-enhanced region, the contrast level in that region will be displayed at its true value. However, when the voxel is larger than the observable contrast agent enhanced area, the displayed image will portray this at a contrast enhancement level that is lower than the true level. At the same time, the location of the contrast-enhanced structure will be accurate to within one resolution unit as to where the enhancement occurred in the subject. To add to this, attenuation levels from the surrounding area – where the contrast agent is not distributed, but still within the volume enclosed by one voxel – affect the effective attenuation (representative CT number) of the volume represented by the voxel. This leads to contrast enhancements of different levels at different sites where the contrast agent localizes.

1.3.3.2 Blood contrast enhancement

The contrast agent most often used for *in vivo* studies is an iodine-based solution. The reason for this is the high x-ray attenuation provided by iodine and the fact that it stays attached to sugar - making it easily tolerated in relatively high concentrations in the blood [38]. The strong attenuation occurs due to the K-edge energy level of iodine (33.2 keV). This value makes for a sharp increase in the attenuation of the x-ray beam at this energy level. This has been tested experimentally by Gomilsek [39].

The distribution of the contrast agent to specific tissues is dependent on the chemical additives bound to the iodine molecule. The combination of iodine and other additives results in a specific size and chemical affinity of the resulting contrast agent.

In the case of blood-pool agents, used for blood and blood vessel enhancement, the chemical additive is only relevant with respect to the size that it induces to prevent the contrast agent from leaking out of the vessels and into the extravascular space as Ritman observed [38]. While this will eventually happen due to the fact that the contrast agent molecule disintegrates in time or is filtered out of the blood by the hepatic glands, for periods longer than the duration of scans, this does

not happen. These types of contrast agents are called blood-pool agents and they are administered through intravenous injections. Clinically used nonionic contrast agents have a short lifetime in the blood, being quickly filtered out [35]. But blood-pool contrast agents used preclinically have been created so that the filtration of the contrast agent is delayed.

One of the common blood-pool agents in preclinical imaging is Fenestra VC with an Iodine concentration of 50 mg/mL. Previous studies [40, 41] have concluded that Fenestra VC gives repeatable enhancement in the blood and so it is a good match for tumour studies due to its long retention in the vasculature [42, 43]. Weichert [44, 45] and Fischbach [46] applied it to rabbit aorta studies and spiral CT angiography respectively, successfully obtaining high levels of enhancement.

Fenestra VC is filtered out of the vasculature and into the liver and spleen. As the contrast level in the vasculature drops, the liver becomes more enhanced. The highest hepatic contrast level enhancement occurs at 24 hours after the administration [42, 43, 47]. Chouker also did a study of vessels within the liver and noticed significant enhancement after the Fenestra VC administration which confirms the distribution and extended duration of Fenetra VC's travel in the blood-stream [48].

1.4 Statement of Thesis

The purpose of this thesis is to characterize the ability of contrast-enhanced micro-CT to identify vascular PDT effects in a RIF-1 tumour implanted in 10-week old C3H mice. The contrast agent enhances the blood contrast over a period of 2 hours after the PDT delivery and by means of late time-point re-administration, blood enhancement is also obtained for the 8 and 24 hour time-point scans. Monitoring the changes in blood over time is done through 8-second micro-CT scans at 8 time-points after treatment. While the purpose of the thesis is not to quantify the vascular volume, ratio measurements of the blood-to-tumour volume take place at ten time-points covering 24 hours after the treatment. The volume measurements are based on summations of all voxels of a CT number expected for contrast-

enhanced blood. The study consists of four study groups – two treated and two untreated. The variation between the PDT treated groups is in the light fluence delivered for PDT, namely 50 and 150 J/cm^2.

Chapter 2

Experimental protocol

2.1 Animal model and tumour cell-line

2.1.1 The mouse model

The subjects in this experiment were female C3H mice (Jackson Laboratories, Bar Harbor, ME, USA) with a mean mass of 23 $\pm$ 2 g. Over the duration of the experiment they were housed in the Animal Resource Centre of the Toronto Medical Discovery Tower (Toronto, Canada). The mice were 11 and 14 weeks old at the time of the cell inoculation and of the treatment respectively. All mouse procedures were in accordance with the ethical approval from the Animal Ethics Committee (University Health Network, Toronto, Canada) and Animal Care Committee (Ryerson University, Toronto, Canada).

2.1.2 The tumour cells

Radiation-induced fibrosarcoma (RIF-1) cells were cultured in Dulbecco's Modified Eagle's Medium and passaged at intervals of 2 – 3 days. For inoculation, a solution of RIF-1 cells and Hank's medium was prepared to contain 10^5 cells per 0.1 mL of solution that was injected. The solution of suspended cells was delivered subcutaneously in the posterior flank of each mouse. At this location, the cells

would grow and multiply to develop into a solid tumour over a period of 3 weeks prior to treatment.

2.2 Treatment procedure and contrast-enhanced micro-computed scanning

2.2.1 Photodynamic therapy

Visudyne (Novartis, Mississauga, Canada) was the vascular photosensitizer used. The photosensitizer dose used was 2 mg per kg of body weight. Before the intravenous injection, the Visudyne dose was diluted in 0.1 mL dextrose.

The light source was a home-made 690 nm diode laser (Princess Margaret Hospital, Toronto, Canada) with maximum power capacity of 300 mW. The light was delivered to the tissue through a 400 μm optical fiber at 100 mW (Fig. 2.1). The light fluence was adjusted by changing the time-exposure of the tissue to the light source achieving 150 and 50 J/cm^2 fluences when reaching the surface of the tumour. The light exposure time was controlled by calculating the exposure necessary for the light fluence used at the tumour surface to stay constant for each tumour with respect to the surface of each particular tumour. This value varied from 3 up to 6 minutes.

The time interval between the delivery of the photosensitizer and the light irradiation was between 15 and 30 minutes. This insured localization of the photosensitizer within the blood vessel at the time of its light activation. The fur covering the tumour was shaved off prior to the experimental protocol to avoid attenuation in the laser beam for arriving at the tumour.

2.2.2 Contrast agent administration

Fenestra VC (ART, Montreal, Canada) containing 50 mg I per mL was delivered via tail-vein injection in a dose of 0.01 mL per g body weight. This dose was

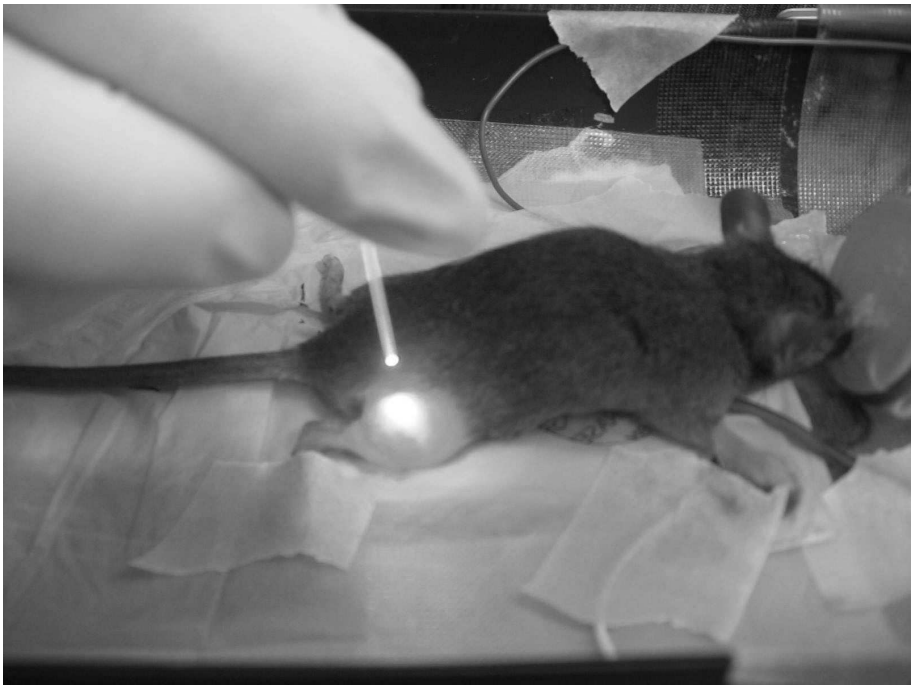

Figure 2.1: A C3H mouse in prone position on the CT table - receiving light irradiation for PDT at the tumour site.

delivered 3 times over the duration of the experiment for each subject – before the 2^{nd}, 9^{th} and 10^{th} scans.

For scans performed approximately 3 hours or longer after the first contrast agent administration [47], another contrast agent dose was delivered prior to the new scan. Hence for the 8- and 24-hour post-PDT scans, the same dose of contrast agent is re-injected. The dose of 0.01 mL per g of body weight proved to give significant contrast enhancement in previous rodent vascular studies [47].

2.2.3 Study groups

The study covered 20 subjects in total, divided into 4 groups (5 subjects each) - 2 treated and 2 untreated. The two PDT-treated groups differed by the light fluence used to activate the photosensitizer administered to each treated subject. One group received a fluence of 150 J/cm^2, while the other received 50 J/cm^2. The variation of the light energy deposition was achieved through varying the time-

exposure of the tumour (*ie.* for the higher fluence group, the tumour was exposed to the laser light for three times as long as the lower fluence subjects).

In order to establish contrast enhancement values and compare PDT effects, two control groups were used. One group received a light-only treatment (150 J/cm^2) instead of PDT and a second group received no treatment. In both control cases, the contrast agent dose was kept the same as in the PDT-treated groups. The purpose of the light-only control group was to allow for comparison of the contrast level in blood in the presence of light irradiation. Table 2.1 summarizes the study groups.

	PDT-treated groups		Control groups	
Group	150 J/cm^2	50 J/cm^2	Light-only	Untreated
Group size	5	5	5	5
Contrast agent (mL/g)	0.01	0.01	0.01	0.01
Light fluence (J/cm^2)	150	50	150	–
Photosensitizer (mg/kg)	2	2	–	–

Table 2.1: The subject groups with their respective PDT and contrast agent parameters. Note: the control groups do not receive photosensitizer.

2.2.4 Scan sequence and photodynamic therapy – timeline

Three weeks after the inoculation of RIF-1 cells, each subject went through a cycle of 10 micro-CT scans. Two were performed prior to treatment: baseline and post-contrast agent scans. After the treatment took place, 8 more scans were performed: 1 immediately following treatment and the others at 0.25, 0.50, 0.75, 1, 2, 8 and 24 hours after treatment. For each of the 8 and 24 hour scans, Fenestra VC was injected once again. The mice were kept under inhaled anaesthesia (1.5% isofluorane in oxygen) during all 10 scans. However, for the first 7 scans, each mouse was anesthetized for approximately 1.5 hours continually and then recovered. For

the last 3 scans, 10 minute anesthetic intervals were sufficient. During the first hour of anesthesia, the subjects' cardiac and pulmonary activity levels along with temperature were monitored using a Biovet physiological monitoring device (m2m Imaging Corp., Cleveland, OH, USA).

	Time
Pre-treatment scans	pre-contrast agent injection
	post-contrast agent injection †
treatment	
Post-treatment scans	immediately after
	0.25 hours
	0.50 hours
	0.75 hours
	1 hour
	2 hours
	8 hours †
	24 hours †

Table 2.2: Experimental timeline. A total of 10 scans is highlighted. Note: † marks the scans which took place within 15 minutes of administering a dose of contrast agent.

2.2.5 Scanning protocol

The micro-CT scanner used was the GE Locus Ultra (General Electric Health Care, London, Canada – Fig. 2.2) housed in the Spatio-Temporal Targeting and Amplification of Radiation Response Center (Medical and Related Sciences Centre, Toronto, Canada). The 8-second scans were performed using 80 kVp and 70 mA anode tube settings with the mouse resting in a prone position. The protocol consisted of 1000 views-per-rotation with a 54-by-54 mm^2 transaxial field-of-view (FOV) . Only the subject-centred volume corresponding to a transaxial area of 40-by-40 mm^2 was reconstructed. The images were reconstructed using an algorithm

similar to Feldkamp's [49] but compensating for the cone-beam geometry, using isotropic voxel spacing of 0.15 mm. The total dose delivered over 10 scans (at 0.06 Gy each) in this study is 0.60 Gy – much below the dose of 6 Gy considered lethal for rodents [40].

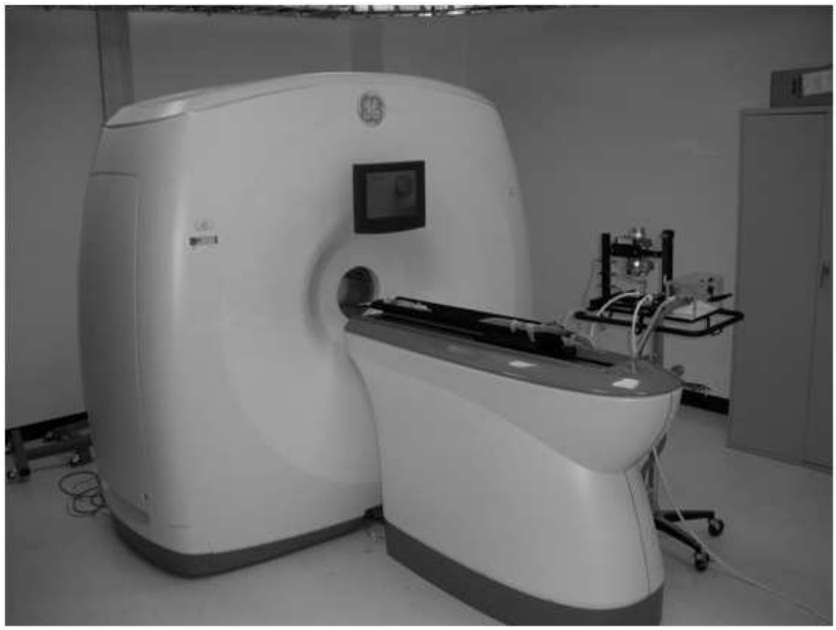

Figure 2.2: The GE Locus Ultra micro-CT scanner.

2.3 Histology and immunohistochemistry

After the 10^{th} scan, each mouse was euthanized by cervical dislocation while still under isofluorane anesthesia. Immediately following this, the necropsy procedure took place. After excision, the tumour was fixed in buffered formalin for 24 hours prior to staining. Central axial slices were then stained with hemotoxin and eosin (H&E).

The H&E staining was used for the purpose of qualitatively identifying if the effects expected through PDT were present or not, to confirm treatment. One subject sample in each group was randomly selected to undergo immunohistochemical

staining (CD31), which allows quantifiable assessment of vascular epithelial damage.

Images of immunostained (CD31) and histological (H&E) slides were taken on a CKX21 microscope with the Olympus IX 71 (Olympus Canada Inc., Markham, Canada) using the QCapture Software (QImaging Corp., Surrey, Canada). Magnification levels used were: 10x, 20x and 40x.

Chapter 3

Image-based measurements of vascular changes

3.1 Image analysis

The image analysis was performed using MicroView 2.2 (General Electric Healthcare, London, Canada), a micro-CT image display and analysis software. In order to quantify vascular changes induced by PDT, comparisons among groups and between scan time-points were performed. The parameter used for comparison was the ratio of contrast-enhanced blood volume-to-tumour volume. This ratio will show the progression of the vascular response as a normalized parameter which overcomes the variation in tumour volume from subject to subject.

The three-dimensional mouse images contain 400 slices, each having a thickness of 0.15 mm. Because the resolution is 0.15 mm, each voxel is representative of a volume of 0.15 x 0.15 x 0.15 mm^3 of the scanned mouse.

3.1.1 Tumour volume by a contouring method

Contouring was used to find the total volume of a region-of-interest (ROI) without excluding any voxel values. By drawing points to delineate the boundary of the ROI in each axial plane of the image and interpolating these contours, a three-

dimensional rendering of the volume enclosed by the contour is generated with the numeric value for the volume given in MicroView.

Whole tumour

In order to avoid any bias in choosing the tumour boundary location based on contrast enhancement of the blood, the contouring was done on the image obtained prior to contrast agent administration. The tumour was first contour-defined in the axial plane direction. The geometry was elliptical in most cases with a few irregularities in some of the subjects. Once the final ROI was obtained, the images for the other 9 time-points were coordinate-registered using the image from the first scan.

Normal tissue adjacent to tumour

The same method was used to contour normal tissue adjacent to tumour. The only difference was in the shape of the ROI. Each adjacent tissue ROI was chosen individually for each tumour scaled to the size of that same tumour.

Bone CT numbers are above the contrast-enhanced blood CT numbers. By selecting the region above the blood threshold (to collect all blood voxels) bone-representative voxels might also be selected if they are found within the same ROI as the blood voxels. For this reason, the slice contours were delineated to include the healthy tissue volume immediately outside the tumour but to exclude bone. The upper boundary (on the border with the tumour) follows the tumour's delimitations. The lower boundary is drawn to match the curvature of the upper boundary while above the femur in all axial planes used. This was done in order to make the procedure repeatable and geometrically consistent among all subjects.

The procedure was based on the tumour ROI contours that were delimited previously. The part of the contour separating the tumour from healthy tissue was left in place. Next, the lower part of the contour outlining the outer boundary of the tumour was moved in a point-by-point manner to become the inner boundary

of the region adjacent to the tumour. This new ROI had a generic banana shape when viewed in the axial plane.

Tumour core and tumour periphery

The contour of the tumour's core was done using the image from the last CT scan (24-hour post-PDT). Then the image from 8-hour post-PDT and pre-PDT scans were coordinate-registered to the original contour image. The overall shape was similar to that of the tumour – elliptical – and the diameter of the core was approximately half of the diameter of the tumour. No contouring was needed for the periphery, as it was obtained by image subtraction of the core from the original tumour. The division line between the core and the periphery was chosen such that the diameter of the core at the widest region was equal to approximately half of the tumour diameter along the same line.

3.1.2 Variability study

One of the downfalls of contouring a three-dimensional image in order to obtain a volumetric ROI is the partial subjective nature of it. This is to say that even using the same image settings another observer would obtain a different volumetric ROI by contouring.

It should be noted that the window settings used in order to visualize the boundary of the tumour properly might be applicable to this tumour type only. Because this method is subject to the analyst's interpretation, the contouring procedure was repeated five more times through an intra- and an inter-observer study.

In this study, image contouring procedure was performed by one observer for a total of three times at intervals of about one month (the intra-observer study). At the same time, the contouring procedure was completed by two other observers – one time each (the inter-observer study). The images analyzed were from the first scan in each of the five untreated subjects, using the same window settings for all images and observers.

3.1.3 Blood volumes in all regions of interest

Firstly, one must identify the CT number range representative of contrast-enhanced blood. Secondly, the total number of voxels with values within that particular CT number range is converted into a volume representative of that type of tissue. The blood volume was found in four ROIs: whole tumour, tumour core, tumour periphery and in the area adjacent to the tumour. Following this, several variations of the ratio of blood volume-to-tissue enclosing blood were calculated for each region.

Finding the blood threshold

In order to find the voxel value representative of blood threshold identification, the image obtained after the first contrast agent injection was used.

The method used for identifying the blood threshold was introduced by Otsu [50]. The algorithm in Otsu's method assumes that a given population of voxels is made of only 2 subpopulations and based on calculations involving a minimal standard deviation from the mean in each subpopulation, the limiting value between the subpopulations is calculated.

Within the tumour, a three-dimensional perimeter was hand-selected such that it would include voxels representative of both tissue and blood (low and high CT number, respectively) in an approximate ratio of one-to-one. These ROIs varied between 376 and 480 voxels, so between 1.27 and 1.62 mm^3.

In this study, the algorithm was utilized independently for each untreated subject obtaining one threshold value for each of the five subjects. The average of these was found to be 100 ± 23 HU, a threshold value that was then applied to all images in the study for blood identification. CT numbers above this threshold are the result of contrast enhancement post contrast agent administration. Therefore, voxels of these values are considered to be representative of blood or vasculature.

In this thesis the term blood voxel is used to refer to a voxel inside the ROI representative of the tumour whose value is 100 HU or more.

Seeded region growing

Once the contrast-enhanced blood threshold is identified, MicroView's seeded region growing function can be used to obtain the contrast-enhanced blood volume.

The contrast-enhanced voxels have a higher CT number value than the background voxels. Therefore, the CT number threshold is chosen to be the lower limit of accepted values in the segmentation algorithm. This means that for a specific threshold and a seed voxel, all voxels neighbouring the seed voxel are considered for selection if they have values greater than or equal to the threshold. The algorithm is iterated on each of these newly added voxels until no more voxels are found that satisfy the positional and threshold conditions. Once the region is complete, the volume is displayed as a sum of the selected voxels through the seeded region growing method.

Variations in blood CT number

The same blood threshold found was used for the seeded region growing procedure at all time-point images analyzed. Variations in CT numbers in a ROI could potentially interfere with the results of the seeded region growing method. In order to monitor this effect, the mean CT number of all 20 subjects at each time-point image is found by the following equation:

$$CT\ number_{mean} = \frac{\sum_{i=1}^{20} CT\ number_i}{20} \tag{3.1}$$

where $CT\ number_i$ is the average CT number in the seeded region grown ROI of blood for each subject at one particular time-point after the contrast injection.

The noise in this ROI or error value for this mean CT number described in Eq. 3.1 is based on the standard deviation in the $CT\ number_i$ in each subject (σ_i) at

the time-point considered:

$$error\ value = \frac{\left(\sum_{i=1}^{20} \sigma_i^2\right)^{1/2}}{20} \tag{3.2}$$

The values for the $CT\ number_{mean}$ at each of the nine time-points after the contrast injection are included in the Table 3.1. They describe the variation in time of the attenuation values within the blood regions.

Scanning time-point pre-PDT (–) or post-PDT (+) (hours)	$CT\ number_{mean}$ (HU)
- 0.25	115 ± 3%
immediately	115 ± 8%
0.25	116 ± 9%
0.50	114 ± 4%
0.75	114 ± 3%
1	118 ± 4%
2	119 ± 5%
8	129 ± 7%
24	139 ± 10%

Table 3.1: Changes in the mean CT number in the blood region in time - all values obtained by Eq. 3.1 and 3.2.

Overall, the error intervals in Table 3.1 indicate that it is acceptable to use the same threshold for identifying blood voxels at all time-points, namely 100 HU.

3.2 Statistical analysis

In order to find the statistical significance of the vascular response, comparisons between groups and between the different time-points were made. The test used was repeated measures ANOVA with Tukey's post-hoc test. The software used for the statistical analysis was Prism 4 (GraphPad Software Inc., San Diego, USA).

3.3 Immunohistochemistry

For one mouse in each study group, the microscope images of CD31 stained tissue taken with a 40x magnification factor (Fig. 3.1a) were converted to threshold-based binary images (Fig. 3.1b) using Adobe Photoshop CS3 (Adobe Systems Inc., San Jose, USA). The CD31 stained areas were those of lowest intensity [51, 52, 53] - the pixels of grey-scale value of zero after the threshold-based conversion. By summing up all pixels of zero grey-scale value (shown in black in Fig. 3.1B), the total CD31 stained area was obtained. This area corresponds to the amount of epithelial coverage.

Finally, a ratio of CD31 stained areas over the total area was calculated. This method is an adaptation from a range of other immunohistochemical studies [54, 55, 56, 57, 58, 59]. An average over three regions in each tumour section was calculated and the four groups were compared.

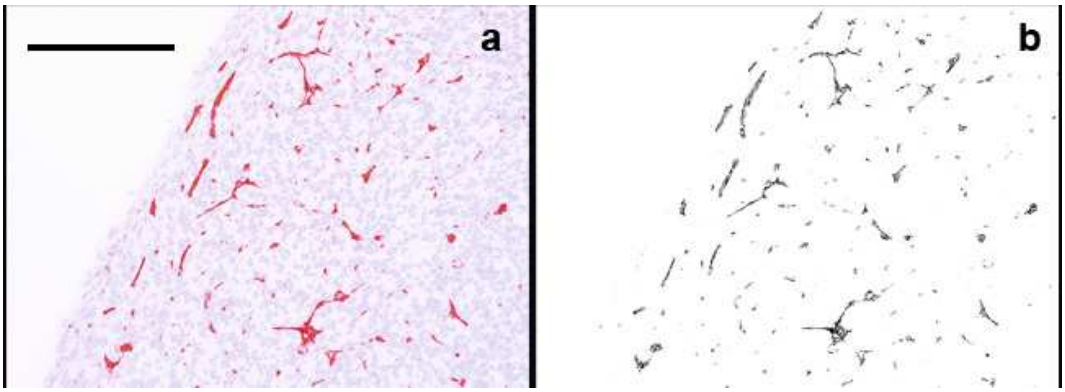

Figure 3.1: An example of the image transformation used for epithelial quantification: (a) Original CD31 stain image (magnification factor: 40x) and (b) The image following the transformation that enhanced the visibility of CD31 stained regions – epithelial cells. The scale bar denotes 100 μm.

Chapter 4

Results and discussion

4.1 Image-based comparison of the vascular response

Changes in vascular response were analyzed in the tumour and in the region adjacent to the tumour. However, in order to establish if the response within the tumour was homogeneous, a more careful look was taken separately at the periphery and at the core.

All results are summarized through Fig. 4.1 to 4.5. The parameter of interest is the ratio of blood volume-to-the region containing that blood volume (*ie.* the tumour blood volume-to-tumour volume or when referring the core of the tumour, the core blood volume-to-core volume). Where necessary, the timeline is broken into two graphs for better visibility of behaviour in the more tightly packed areas. All graphs show error bars representative of the standard error within each group at each time-point. The source of this is the variation in the ratio mentioned above from subject to subject.

4.1.1 Overall changes within the tumour

Comparisons within each group

Comparisons of each post-PDT time-point ratio to the pre-PDT time-point ratio, within each group, indicate that the 150 J/cm^2 PDT group and the 50 J/cm^2 PDT group show significant changes in tumour ratio of blood-to-full ROI volume in time. This change is significant at the 2-, 8- and 24-hour post-PDT time-point for 150 J/cm^2 PDT ($p < 0.01$) and at the 24-hour post-PDT time-point for 50 J/cm^2 PDT ($p < 0.05$).

The two control groups also showed significant blood volume change at the 24-hour post-PDT time-point when compared to the pre-PDT time-point ($p < 0.05$). The control groups might be exhibiting the results of natural development in tumour ratio of blood-to-full ROI volume over time [60]. Another possibility is that previously injected contrast agent leaked out of the vessels. After entering into the extravascular space, it became unable to return to the vessel. So by an additional contrast agent dose administration, the effect could have been additive on the image obtained. Another explanation could be a variation in the true value of enhancement in the first hour of scans. During first one hour of scans, the subjects were under anesthetic, which would result in a lower heart rate. A drop of blood contrast enhancement would follow due to a potentially low distribution rate of contrast agent in the tumour [61]. All data can be observed in Fig. 4.1.

Comparison between groups

Of all the time-points compared, the only ones to show significant difference between groups were at the 2-, 8- and 24-hour time-points. This can be observed in Fig. 4.1. Only the 150 J/cm^2 PDT group was found to have a significantly higher ratio of blood-to-full ROI compared to all the other three groups: at 2-hours post-PDT ($p < 0.05$), at 8-hours post-PDT ($p < 0.01$) and at 24-hours post-PDT ($p < 0.01$). An example of the difference between the tumour vascular response among the groups is also given in Fig. 4.2 (axial slices of the 24-hour post-PDT images of

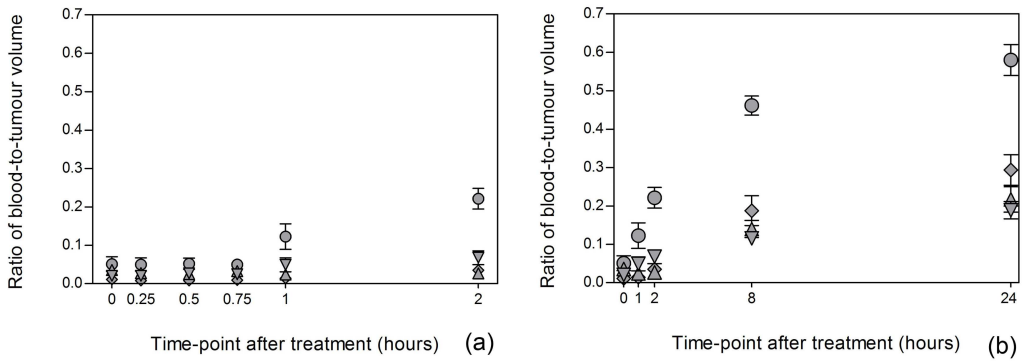

Figure 4.1: Tumour ratio of blood-to-full ROI volume in the four study groups post-PDT: (a) immediately post-PDT up to 2 hours post-PDT and (b) immediately post-PDT up to 24 hours post-PDT (hourly time-points only). Legend: (◯) 150 J/cm^2 PDT, (♢) 50 J/cm^2 PDT, (△) 150 J/cm^2 light-only and (▽) untreated.

a sample subject from each group are shown).

4.1.2 Tumour core versus tumour peripheral changes

There is a possibility that some vascular effects are distinguishable at the 8- and 24-hour post-PDT time-point for the 50 J/cm^2 PDT group also; but due to averaging effects over the entire tumour they could have been missed. Therefore separate comparisons were done to verify variations in time or among groups in the core and the periphery of the tumour separately.

Comparisons within each group

Overall. In each group, comparisons were drawn at each time-point, between each two of three regions - the core, the periphery and the total tumour volume (core + periphery). None of the four groups showed any difference between the three regions at any of the three time-points tested (pre-PDT, 8- and 24-hour post-PDT). Fig. 4.3 illustrates the results for: (a) 150 J/cm^2 PDT, (b) 50 J/cm^2 PDT, (c) 150 J/cm^2 light-only and (d) untreated.

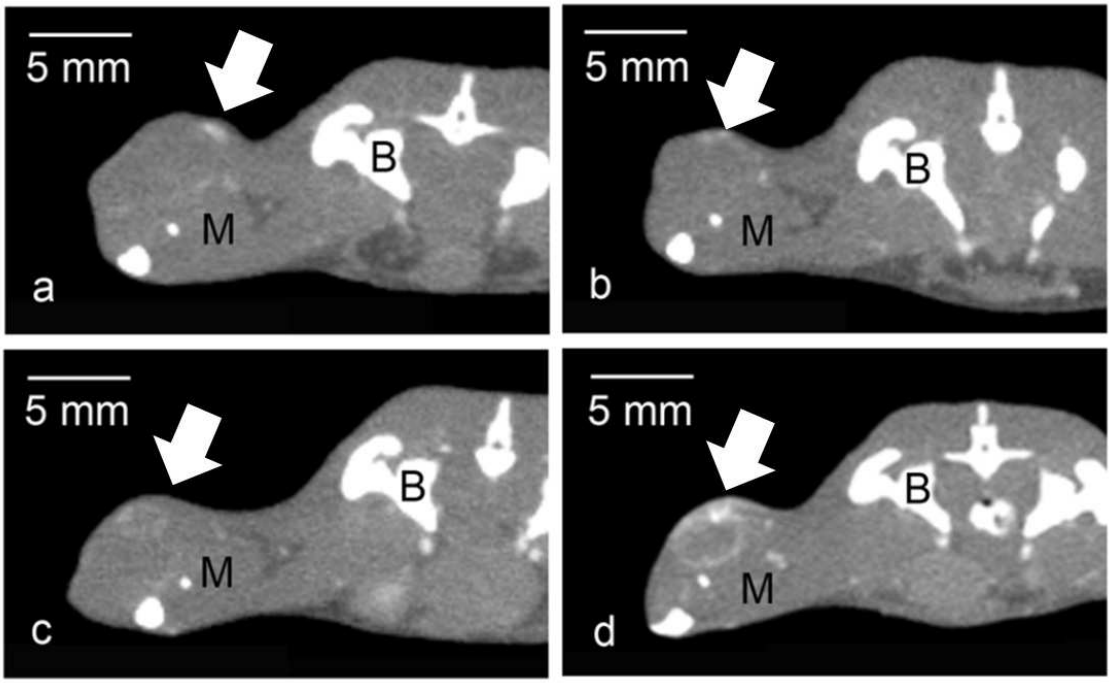

Figure 4.2: Sample axial view of a mouse in each study group (at the 24 hour post-PDT time-point). (a) untreated, (b) 150 J/cm^2 light-only, (c) 50 J/cm^2 PDT, and (d) 150 J/cm^2 PDT. Note: all images have isotropic voxel spacing of 0.15 mm.

In the peripheral region. The ratio of blood-to-full ROI volume data in the periphery of the tumour is illustrated in Fig. 4.4a. In each group, the ratios obtained from the pre-PDT, the 8- and the 24-hour post-PDT scans were compared. In the 150 J/cm^2 PDT group, the 8- and 24-hour post-PDT ratios were significantly higher than the pre-PDT ratio ($p < 0.01$). The same occurred in the 50 J/cm^2 PDT group ($p < 0.05$). No ratio change was detected in the two control groups ($p > 0.05$).

In the core region. For all four groups, the ratio of blood-to-full ROI volume for the core of the tumour is illustrated in Fig. 4.4b. The ratio of blood-to-full ROI volume in the 150 J/cm^2 PDT group was significantly higher for the 8- and 24-hour post-PDT time-point when compared to the pre-PDT ratio ($p < 0.05$ and

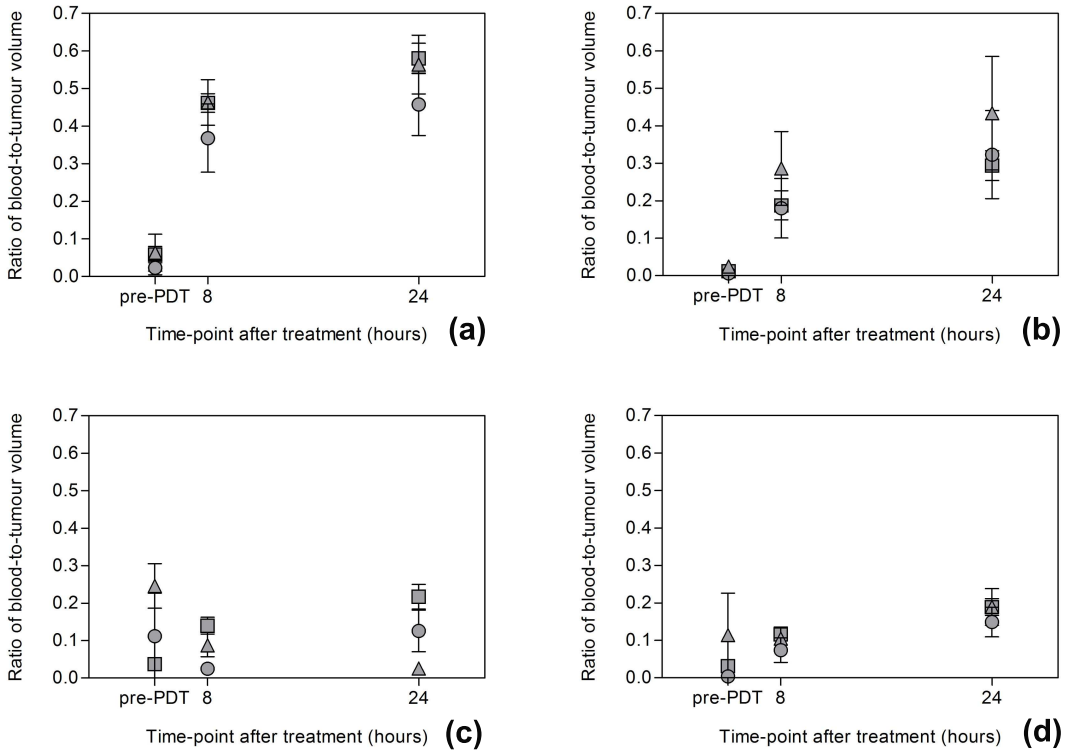

Figure 4.3: Treatment groups – (◯) core, (△) periphery and (□) cumulative ratio of blood-to-full ROI volume levels pre-PDT and 8-hours and 24-hours post-PDT: (a) 150 J/cm^2 PDT, (b) 50 J/cm^2 PDT, (c) 150 J/cm^2 light-only and (d) untreated.

$p < 0.01$ respectively). The ratio remained unchanged in the control and in the 50 J/cm^2 PDT groups ($p > 0.05$).

Comparisons between groups

The comparison is done between the groups at each of the 8- and 24-hour post-PDT time-points.

In the peripheral region. The ratio of blood-to-full ROI volume in the tumour periphery was significantly higher in the 150 J/cm^2 PDT group when compared to all the other three groups. The 8-hour post-PDT ratio was higher when compared to the 50 J/cm^2 PDT ($p < 0.01$) and to the two control groups ($p < 0.001$). The 24-hour post-PDT ratio was higher when compared to the 50 J/cm^2 PDT ($p < 0.01$), to the 150 J/cm^2 light-only ($p < 0.01$) and to the untreated ($p < 0.001$) groups. All results are illustrated in Fig. 4.4a).

In the core region. The 150 J/cm^2 PDT group was found to be significantly higher than the untreated groups at the 8- and 24-hour post-PDT time-points ($p < 0.05$).

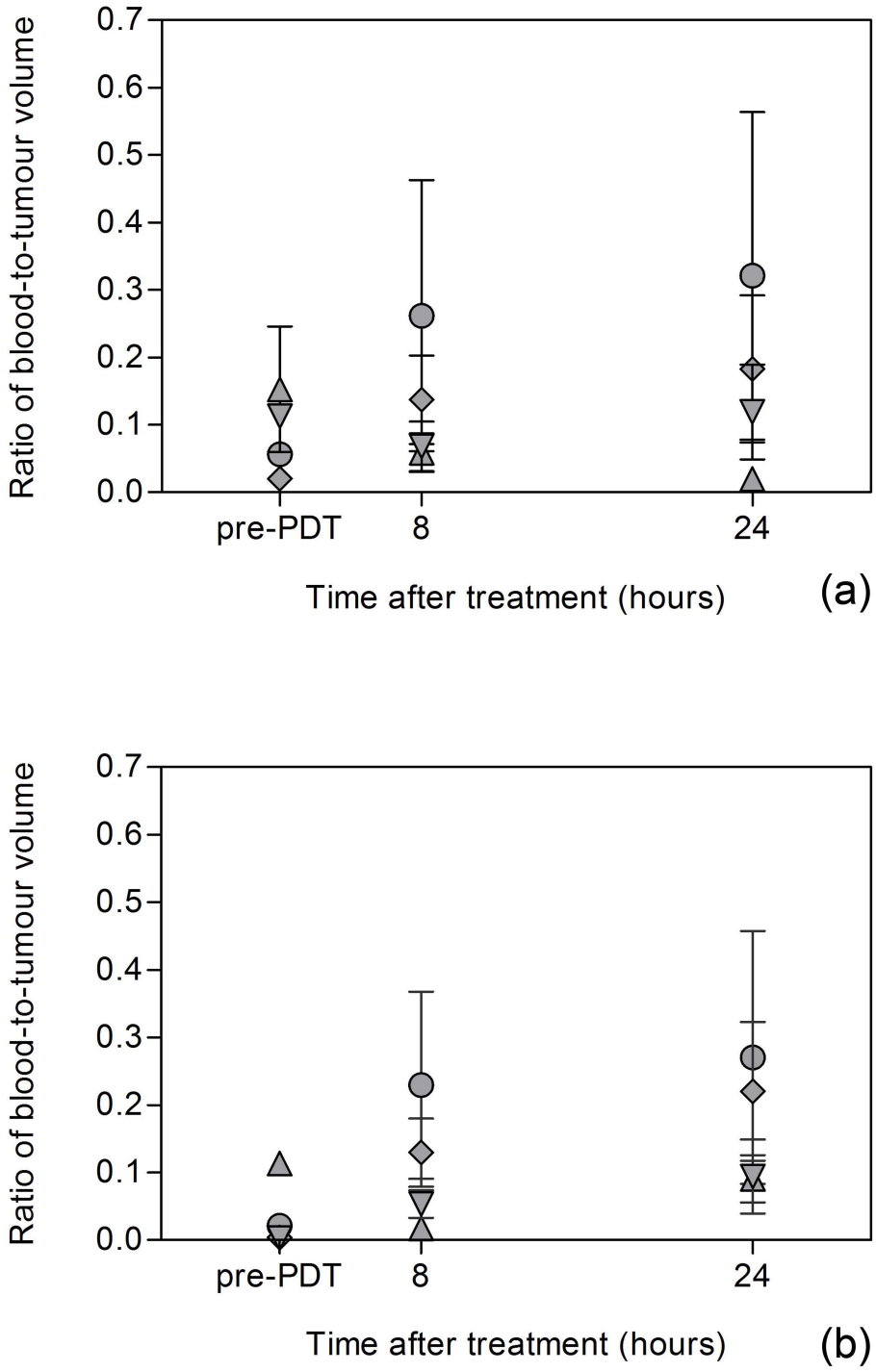

Figure 4.4: Tumour peripheral (a) and core (b) ratio of blood-to-full ROI volume – pre-PDT, 8-hours and 24-hours post-PDT. Legend: (◯) 150 J/cm^2 PDT, (◇) 50 J/cm^2 PDT, (△) 150 J/cm^2 light-only and (▽) untreated.

4.1.3 Changes in the tissue adjacent to the tumour

No blood volume changes were observed as occurring in time in any of the four groups. When comparing the groups at each time-point, no significant difference was observed (Fig. 4.5).

The post-PDT time-point images and the pre-PDT within each group were compared. For each time-point, a comparison between the treated groups and the control groups was done. Neither test showed any change in blood volume in time within each group ($p > 0.05$) nor among groups at each time-point ($p > 0.05$). As expected [7], the healthy tissue surrounding the tumour was not affected by the PDT.

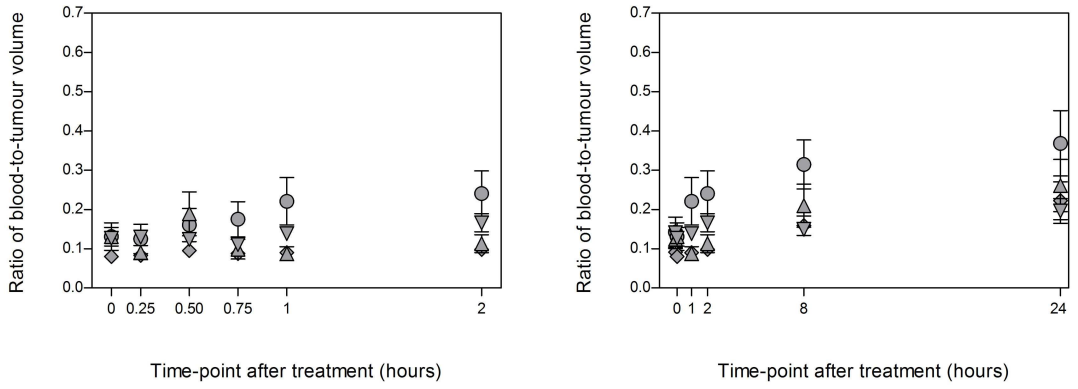

Figure 4.5: The ratio of blood-to-full ROI volume in the tissue adjacent to the tumour post-PDT: (a) immediately post-PDT up to 2 hours post-PDT and (b) immediately post-PDT up to 24 hours post-PDT (hourly time-points only). Legend: (◯) 150 J/cm^2 PDT, (◇) 50 J/cm^2 PDT, (△) 150 J/cm^2 light-only and (▽) untreated.

4.2 Variability study

In the intra-observer study, the mean volume was obtained from the three repeated measurements for each tumour in the untreated group. The standard deviation for the five untreated tumours varied between 3% and 8%. In the inter-observer study, the standard deviation among the observations of three observers for each of the

untreated mice was between 10% and 30%. The results are presented in detail in Table 4.1.

Untreated subject	Intra-observer	Inter-observer
	mean and standard deviation (mm^3)	
Case 1	160.61 ± 5.55	139.02 ± 27.80
Case 2	67.45 ± 5.67	76.05 ± 10.49
Case 3	112.32 ± 9.04	117.28 ± 27.53
Case 4	55.58 ± 2.11	45.10 ± 14.55
Case 5	173.79 ± 5.54	127.12 ± 26.63

Table 4.1: The results of contouring the tumour volume in the variability study.

4.3 *Ex vivo* immunohistochemical results

The histology slides, representative of the tissue properties at 24 hours after treatment, showed evidence of treatment in the two treated groups (Fig. 4.6). The results obtained from the CD31-based method (Fig. 4.7) are in agreement with literature. The same trend of decreased amount of epithelium following PDT was also observed immunohistochemically in other studies [56, 53, 59].

More specifically, the high fluence PDT group had the lowest ratio of epithelial area-to-total tissue out of all groups, namely 3% ± 2%. The standard error in all groups was 2 – 5%. This makes the low fluence PDT and the light-only group indistinguishable at values of 14% ± 3% and 11% ± 5% respectively. Lastly, the control group showed a ratio of epithelial area-to-total tissue of 29% ± 5%, which when compared to the high fluence PDT indicates a lack of epithelial effects in the tumour vasculature at the 24 hour time-point.

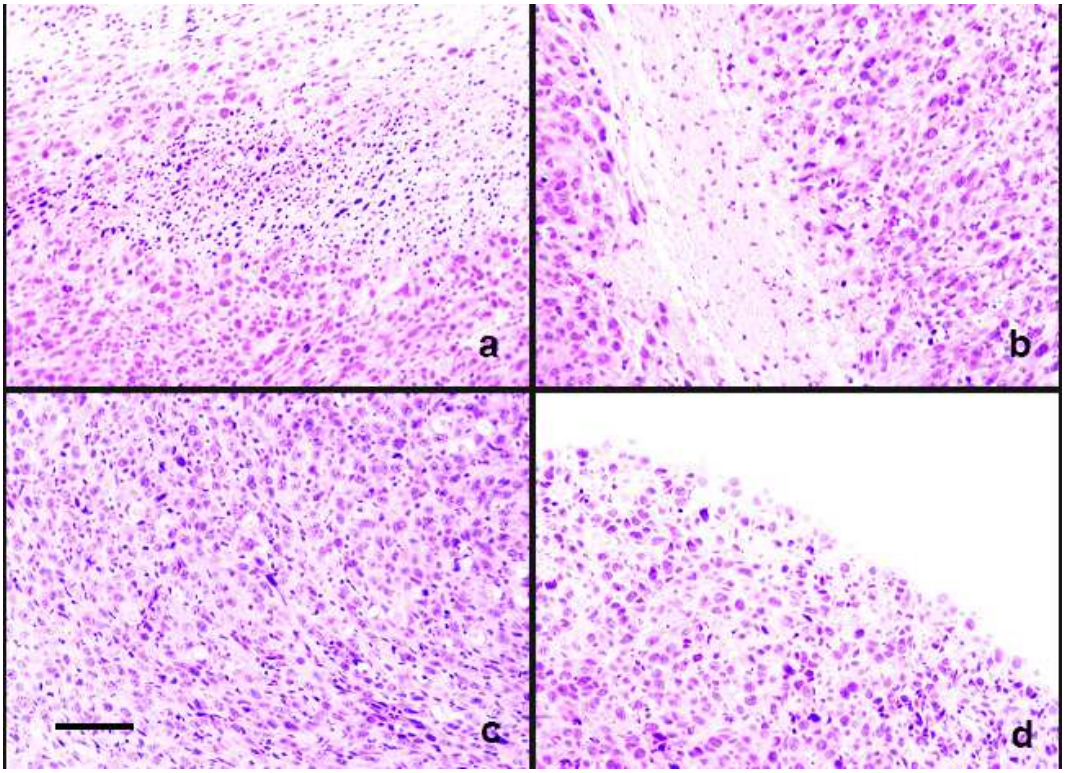

Figure 4.6: H&E staining of a tissue sample slice at 24 hours post-PDT: (a) 150 J/cm^2 PDT, (b) 50 J/cm^2 PDT, (c) 150 J/cm^2 light-only and (d) untreated. Note: 20x magnification factor. The scale bar denotes 100 μm.

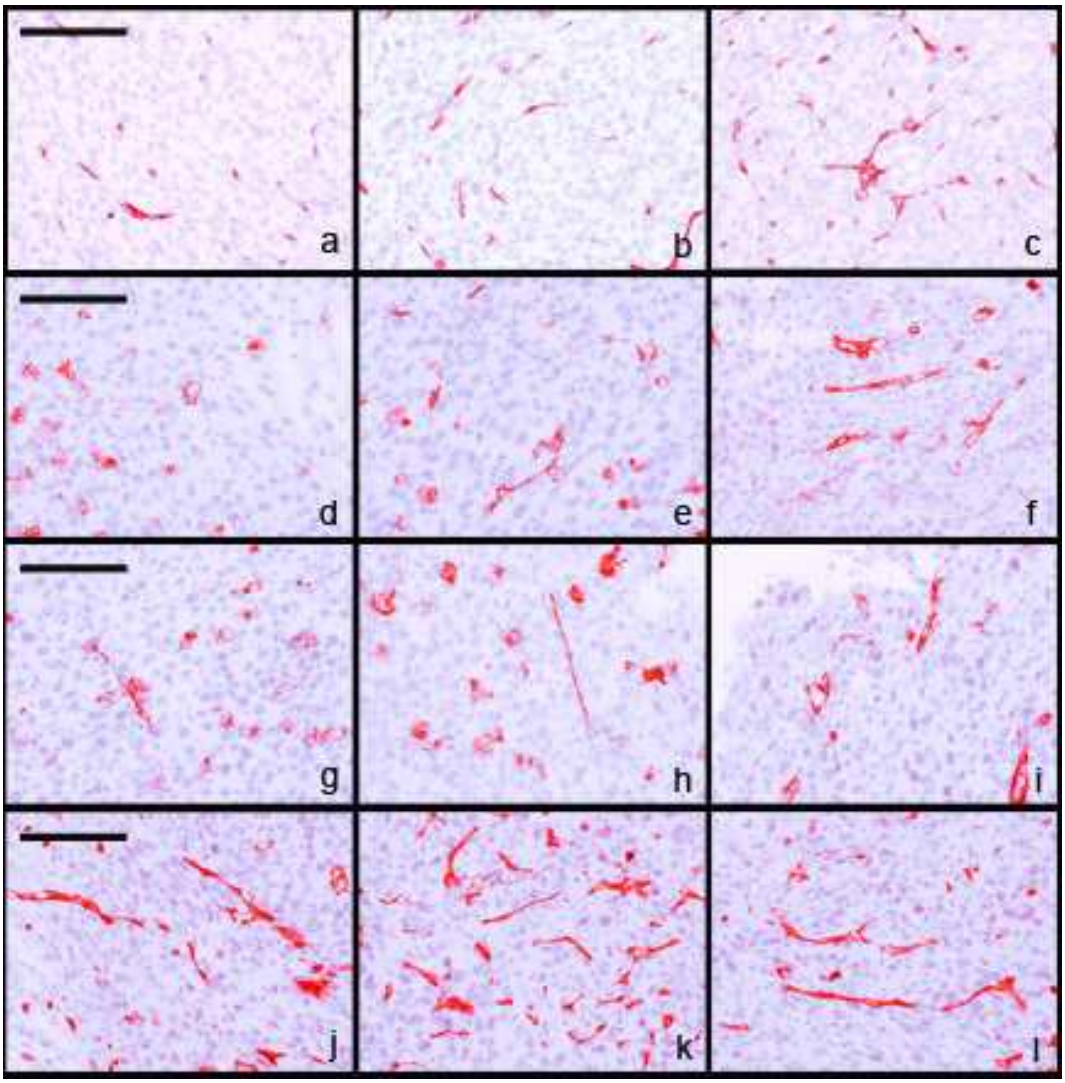

Figure 4.7: CD31 staining of a tissue sample slice at 24 hours post-PDT: (a – c) 150 J/cm^2 PDT, (d – f) 50 J/cm^2 PDT, (g – i) 150 J/cm^2 light-only and (j – l) untreated. Note: 40x magnification factor. The scale bar denotes 100 μm.

4.4 Discussion

Vascular effects can vary in different types of tumour as well as by varying PDT parameters (*ie.* laser irradiance-photosensitizer delivery interval, total energy deposited in the tissue). Therefore, for comparing results one needs to look at cases that come as close as possible to the ones used in the case study.

The literature chosen for comparison in this study, describes vascular PDT effects in the same tumour cell line using similar PDT parameters. Some studies have isolated regions within the tumour to monitor with *in vivo* markers or by other imaging techniques. By looking at some selective 2-D planes by ultrasound, optical coherence tomography [62] or fluorescent staining [63, 2], the response to PDT was determined. Some of these studies also attempted to give a time profile of the response; the downfall here was in not using the exact location at the later time-points after the subject has been moved.

Some studies also used a control group that received photosensitizer-only and in the absence of light [8, 64, 69]. This choice is of value in studies where the method allows imaging this substance *in vivo* in order to compare it with the results of imaging the PDT treated group using the same imaging method. One example of this is when using fluorescent-labelled substances to trace the photosensitizer using PET scans. In such a study [64] the decision between a photosensitizer-only and a light-only group was made knowing that neither method caused any effects in the tissue . However, when imaging with micro-CT, this type of a control group would not be of use. Considering that its chemical make-up does not include Iodine or Gadolinium, its presence in the blood would go unnoticed in the micro-CT images. Another potential reason for using the photosensitizer-only control group in a PET study is that one can use one subject as both control and PDT treatment. This can be achieved by implanting 2 tumours, and while the photosensitizer is delivered to both tumours, by only irradiating one of them, the other is kept as control (photosensitizer-only control). But as before, this aspect is only useful in the case of PET where the use of a fluorescent label, allows for imaging both groups. And

this would not translate to micro-CT.

As expected, the 150 J/cm^2 PDT group showed the strongest response when compared to the control groups. However, instead of seeing a decrease in the ratio of blood-to-tumour volume as noted in other studies, an increase was noticed. In several other studies, the parameters monitored were blood flow [6, 8, 65, 66], blood volume [6] and perfusion [67, 68] – which were shown to decrease in time – be it at 3, 6 or 24 hours. No study yet has been able to confirm complete blockage of all vessels in the tumour following PDT as current devices able to monitor blood flow have a lower speed limit of detection of blood flow. Another vascular PDT effect is increased vessel permeability [69, 8] due to vessel dilation [6] and destruction of epithelial cells in the vessel walls. Therefore, blood (along with contrast-agent) could leak out from the tumour vessels into the extravascular space creating enhancement where no vessel was present. With the volume of contrast agent introduced at 8 and 24 hours after treatment, a higher local dose of contrast agent at the site of the tumour will manifest as an increase in volume of contrast-enhanced blood. All of the above cause local contrast-enhancements which are not localized within the tumour vasculature, especially at 8 and 24 hours post-PDT due the re-administration of contrast agent. This decrease in vessel epithelial area (vessel damage) in the 150 J/cm^2 PDT group was confirmed by immunohistochemistry (CD31 staining). This stain indicated a smaller ratio of epithelial area-to-tissue area in the 150 J/cm^2 PDT group at the 24 hour time-point when the sample was collected.

The 50 J/cm^2 PDT group did not show significantly different results from the control groups. The effects of low light fluence PDT were confirmed histologically and the effects were distinguishable from the high light fluence PDT. Immunohistochemically, looking at the area of vascular epithelial coverage, the results were indicative of similarities existing between the 50 J/cm^2 PDT group and the control groups in terms of the scale of the effects occurring. There is no discordance per se between the *in vivo* and *ex vivo* histology results at the 24 hour time-point. The interpretation lies in this discordance translating into contrast-enhanced micro-CT

not being able to monitor the magnitude of small scale effects. While other studies claim to be monitoring effects as soon as 2 hours after PDT, there is a combination of two potential reasons why this is not observable by contrast-enhanced micro-CT. Other than the small magnitude of the vascular PDT effects in the 5-11 μm wide vessels [60, 70] in the case of low fluence PDT, there is the issue of resolution of the scanner undermining the ability to observe any changes due to partial volume effects [36, 37].

With respect to the results related to core and periphery of tumours, the interpretations can only be speculative as no other imaging studies have broken down PDT effects in this manner. Hence, looking strictly on the biological side, the RIF-1 tumour is known to be highly vascularized at both the core and the periphery – the peripheral area being slightly richer in blood volume than the core [68]. The periphery effects are shown to be observable with contrast-enhanced micro-CT at the later time-points (8 and 24 hours post-PDT) in both PDT groups when compared to the blood volume level before PDT. For the core, an increase in the ratio of blood volume-to-core volume in time occurs in the higher fluence PDT group. Since the vascularization levels are similar in the core and periphery, these results are not surprising. The reason why a greater effect is not observed is the fact that light of lower intensities reach the core and reducing the effects in this region. At the same time, it is possible that the maximal effects, occurring in the periphery leading to permeability of vessels [69, 8] at as soon as 2 hours after PDT, are indirectly causing the appearance of an effect at the core. It is possible that increased permeability in peripheral vessels allows leakage of contrast agent from peripheral vessels into the core extravascular space. And so, the core contrast enhancement might not be the effect of PDT on core vasculature, but the side-effects of PDT on the periphery. In other words, it is possible that the localization of the contrast-enhanced voxels is not in the vessels at all. This explains the change noticed at the core and the fact that the effects are stronger in the higher fluence PDT group.

The lack of changes in the volume adjacent to the tumour only serves to confirm that the PDT effects did not take place anywhere else outside the tumour [4]. By

delivering of the light at a low enough fluence, the vascular effects are limited to the tumoural site. Current studies are undergoing to create photosensitizer that not only bind to epithelial cells but also use antibody encoding for binding to specific locations of these vessels in the body such as in tumours [71].

4.4.1 Limitations of contrast-enhanced micro-computed tomography imaging

The contrast-enhancement technique is time-restrictive in the clinical world because of the short lifetime of the contrast media used for imaging vascular enhancement. Preclinical studies have characterized levels of enhancements and correlated these with blood-pool contrast agent concentrations and body weight in a longitudinal manner.

At the preclinical level, some limitations still remain. Spatially, when smaller structures are imaged, namely smaller than the limiting resolution of the scanner, lower values than the true contrast enhancement values are displayed, giving an inaccurate picture of the location and magnitude of vascular effects. Temporally, contrast enhancement is a function of time due to the physiological filtration mechanisms clearing the contrast agent out of the vessel lumen.

Some studies using flat-panel detector micro-CT scanner used similar scanning resolutions [72, 73] in imaging small animals. For example Jorgensen had access to a scanner which allowed for scans of specimens where structures of 25 μm were resolved [74]. Blood vessels in the RIF-1 tumour reach in size below 25 μm [60] hence a voxel that is 150 μm wide might not capture and resolve all of these contrast-enhanced vessels.

While longitudinally, the limitations are surpassed by re-injecting the contrast agent, the scanner resolution might affect the results of this study. The GE Locus Ultra scanner is capable of dynamic imaging through high speed data collection in 1 – 16 seconds [72, 75, 76], but the resulting isotropic voxel spacing is of 150 μm. Ritman observed [61] that a minimum of 100 μm isotropic voxel is necessary

in order for the image quality of micro-CT scanners to be comparable to that of clinical scanners. However, in the case of a longitudinal study like this one, contrast-enhanced structure changes in time are the observables. For this purpose, exact rendering of vascular structures is not a priority.

Chapter 5

Conclusion and future directions

5.1 Conclusion

This study shows that contrast-enhanced micro-computed tomography is a feasible tool to monitor vascular changes induced by photodynamic therapy in time in a three-dimensional manner. The response was strongest in the high fluence PDT group at the late time-points 8 and 24 hours after the treatment – moreso in the periphery of the tumour as compared to the core. The physiological event linked to the observations of the study is vascular permeability. The current limitation preventing an absolute quantification of blood volume is the partial volume effect induced by the combination of blood vessel size and limiting resolution of the scanner.

5.2 Future directions

Permeability of the vessels could be further tested by keeping the current study parameters and adding scanning timepoints to the protocols at specific times. For example performing one scan before the contrast agent administration at the 8 and 24 hour timepoints would allow for assessment of contrast agent that has permeated into the extravascular space during the first 2 hours of scanning. This value could

be used in order to normalize the value calculated in the image after the contrast agent administration.

Partial volume effects currently limit the interpretation of the results. But in order to address questions related to this topic, another scan could be added to the protocol. This would be performed immediately after euthanasia and after the injection of *post mortem* contrast agent. The scanner used for this step would be one of high dose and high resolution (currently capable of reaching 25 μm resolution images). The x-ray dose would not be a problem at this timepoint and the high resolution would permit better visualization of the vascular network.

This study could be propagated further in several directions – be it by varying PDT parameters or imaging parameters and by introducing monitoring time-points past 24 hours – in order to better understand the relationship between tissue types, treatment and diagnostic x-ray attenuation. A study of the change in effects with such variations of parameters would help in making predictions and extend the results to other types of tumours without the need for repetitive experiments.

5.2.1 Limiting imaging resolution

An important factor in identifying blood voxels within the tumour was the threshold value. This value was a function of incident beam energy, the size of the structure being resolved, the linear attenuation coefficient of the structure monitored and the limiting resolution of the scanner. It is possible that a change in any of the above parameters would induce a blood threshold change. But the effects of partial volume as a function of the scanner resolution and the size of the structure monitored would still affect the imaging results. By introducing a 24-hour post-treatment imaging sequence of just the tumour sample, using a higher resolution scanner typically used for *post mortem* samples, it would be possible to complete the picture of identifying the specific events occurring at that time-point.

5.2.2 Tumour type and location

Different tumours with different levels of vascularization will respond to treatment in different ways, which will translate into differences in the contrast-enhanced micro-CT images obtained. The location of the tumour could require interstitial delivery of the light dose for more efficient activation of the photosensitizer. Such changes in the tumour type and treatment delivery will also result in a variation of tumour response which would once again translate into a change in the contrast-enhanced micro-CT images generated in such experiments. By performing a study where the same PDT parameters are used on two different types and locations of tumours (one internal and one superficial), the image parameters would be better understood as linked to type and location of tumour.

Bibliography

[1] Stanley S. Stylli and Andrew H. Kaye. Photodynamic therapy of cerebral glioma - A review Part I - A biological basis. *Journal of Clinical Neuroscience*, 13(6):615 – 625, 2006.

[2] L. A. Sporn and T. H. Foster. Photofrin and light induces microtubule depolymerization in cultured human endothelial cells. *Cancer Research*, 52(12):3443–3448, 1992.

[3] T. H. Foster, R. S. Murant, R. G. Bryant, R. S. Knox, S. L. Gibson, and R. Hilf. Oxygen consumption and diffusion effects in photodynamic therapy. *Radiation Research*, 126(3):296–303, 1991.

[4] A. M. Richter, A. K. Jain, A. J. Canaan, E. Waterfield, E. D. Sternberg, and J. G. Levy. Photosensitizing efficiency of two regioisomers of the benzoporphyrin derivative monoacid ring A (BPD-MA).

[5] K. Ichikawa, Y. Takeuchi, S. Yonezawa, T. Hikita, K. Kurohane, Y. Namba, and N. Oku. Antiangiogenic photodynamic therapy (PDT) using Visudyne causes effective suppression of tumor growth. *Cancer Letters*, 205(1):39–48, 2004.

[6] T. Osaki, S. Takagi, Y. Hoshino, M. Okumura, and T. Fujinaga. Antitumor effects and blood flow dynamics after photodynamic therapy using benzoporphyrin derivative monoacid ring A in KLN205 and LM8 mouse tumor models. *Cancer Letters*, 248(1):47–57, 2007.

[7] B. Chen, Y. Xu, T. Roskams, E. Delaey, P. Agostinis, J. R. Vandenheede, and P. de Witte. Efficacy of antitumoral photodynamic therapy with hypericin: Relationship between biodistribution and photodynamic effects in the RIF-1 mouse tumor model. *International Journal of Cancer*, 93(2):275–282, 2001.

[8] B. Chen, B. W. Pogue, I. A. Goodwin, J. A. O'Hara, C. M. Wilmot, J. E. Hutchins, P. J. Hoopes, and T. Hasan. Blood flow dynamics after photodynamic therapy with verteporfin in the RIF-1 tumor. *Radiation Research*, 160(4):452–459, 2003.

[9] Stanley S. Stylli and Andrew H. Kaye. Photodynamic therapy of cerebral glioma - A review Part II - Clinical studies. *Journal of Clinical Neuroscience*, 13(7):709 – 717, 2006.

[10] R. Veenhuizen, H. Oppelaar, M. Ruevekamp, J. Schellens, O. Dalesio, and F. Stewart. Does tumour uptake of foscan determine PDT efficacy? *International Journal of Cancer*, 73(2):236–239, 1997.

[11] T. M. Sitnik, J. A. Hampton, and B. W. Henderson. Reduction of tumour oxygenation during and after photodynamic therapy in vivo: effects of fluence rate. *British Journal of Cancer*, 77(9):1386–1394, 1998.

[12] V. H. Fingar, T. J. Wieman, Y. J. Park, and B. W. Henderson. Implications of a pre-existing tumor hypoxic fraction on photodynamic therapy. *Journal of Surgical Research*, 53(5):524–528, 1992.

[13] R. Gillies, N. Kollias, T. Hasan, and H. Diddens. Spectral characterization of the benzoporphyrin derivative monoacid ring-A photoproduct formed in fetal calf solutions during irradiation with 694 nm continuous-wave radiation. *Journal of Photochemistry and Photobiology B-Biology*, 35(3):247–247, 1996.

[14] Robert S. Kerbel Peter N. Burns F. Stuart Foster David E. Goertz, Joanne L. Yu. High-frequency Doppler ultrasound monitors the effects of antivascular therapy on tumor blood flow. *Cancer Research*, 62(22):6371–5, 2002.

[15] C. K. Hitzenberger A. F. Fercher, W. Drexler and T. Lasser. Optical coherence tomographyprinciples and applications. *Reports on Progress in Physics*, 66:239–303, 2003.

[16] Jerrold T. Bushberg et. al. The Essential Physics of Medical Imaging. *Medical Physics*, 30(7):1936–1936, 2003.

[17] E. L. Ritman. Micro-computed tomography-current status and developments. *Annual Review of Biomedical Engineering*, 6:185–208, 2004.

[18] M. J. Paulus, S. S. Gleason, S. J. Kennel, P. R. Hunsicker, and D. K. Johnson. High resolution X-ray computed tomography: An emerging tool for small animal cancer research. *Neoplasia*, 2(1-2):62–70, 2000.

[19] L. Axel. Cerebral blood-flow determination by rapid-sequence computed tomography - a theoretical analysis. *Radiology*, 137(3):679–686, 1980.

[20] C. T. Badea, M. Drangova, D. W. Holdsworth, and G. A. Johnson. In vivo small-animal imaging using micro-CT and digital subtraction angiography. *Physics in Medicine and Biology*, 53(19):R319–R350, 2008.

[21] J. P. Schlomka, E. Roessl, R. Dorscheid, S. Dill, G. Martens, T. Istel, C. Baumer, C. Herrmann, R. Steadman, G. Zeitler, A. Livne, and R. Proksa. Experimental feasibility of multi-energy photon-counting K-edge imaging in pre-clinical computed tomography. *Physics in Medicine and Biology*, 53(15):4031–4047, 2008.

[22] P. Sukovic and N. H. Clinthorne. Basis material decomposition using triple - Energy X-ray computed tomography. *Imtc/99: Proceedings of the 16th IEEE Instrumentation and Measurement Technology Conference, Vols. 1-3*, pages 1615–1618, 1999.

[23] E. Roessl and R. Proksa. K-edge imaging in x-ray computed tomography using multi-bin photon counting detectors. *Physics in Medicine and Biology*, 52(15):4679–4696, 2007.

[24] Thorsten M. Buzug. *Computed tomography: from photon statistics to modern cone-beam CT*. Springer, Berlin, 2008.

[25] Ronald Bruening. *Protocols for multislice CT*. Springer, New York, 2006.

[26] Euclid Seeram. *Computed tomography: physical principles, clinical applications, and quality control*. W.B. Saunders, Philadelphia, 2001.

[27] M. Torikoshi, T. Tsunoo, M. Sasaki, M. Endo, Y. Noda, Y. Ohno, T. Kohno, K. Hyodo, K. Uesugi, and N. Yagi. Electron density measurement with dual-energy x-ray CT using synchrotron radiation. *Physics in Medicine and Biology*, 48(5):673–685, 2003.

[28] S. K. Carlson, K. L. Classic, C. E. Bender, and S. J. Russell. Small animal absorbed radiation dose from serial micro-computed tomography imaging. *Molecular Imaging and Biology*, 9(2):78–82, 2007.

[29] John M. Boone, Orlando Velazquez, and Simon R. Cherry. Small-animal X-ray dose from micro-CT. *Mol Imaging*, 3(3):149–58, 2004.

[30] R.F. Kallman H.I. Kohn. The influence of strain on acute X-ray lethality in the mouse I. LD50 and death rate studies. *Radiat Res.*, 5:309–317, 1956.

[31] N. Kawashima F. Chino F. Sato, Sasaki S. Late effects of whole or partial body X-irradiation on mice: Life shortening. *Int. J. Radiat. Biol. Relat. Stud. Phys. Chem. Med.*, 39:607–615, 1981.

[32] J.S. Robertson V.P. Bond. Vertebrate Radiobiology (Lethal Actions and Associated Effects). *Annual Review of Nuclear Science*, 7:135–162, 1981.

[33] R.H. Mole. Quantitative observations on recovery from whole body irradiation in mice II. Recovery during and after daily irradiation. *Br J Radiol.*, pages 40–46, 1957.

[34] F. A. Dilmanian, X. Y. Wu, J. Kress, B. Ren, D. Chapman, J. A. Coderre, D. Greenberg, E. Parsons, M. Shleifer, D. N. Slatkin, W. C. Thomlinson, Z. Zhong, T. M. Button, F. Giron, J. Liang, M. J. Petersen, C. T. Roque, M. H. Miller, H. Weedon, D. J. Krus, L. Perna, and K. Yamamoto. Dual energy iodine contrast CT with monochromatic x-rays. *1995 IEEE Nuclear Science Symposium and Medical Imaging Conference Record, Vols 1-3*, pages 1392–1396, 1996.

[35] Guy Marchal et al. *Multidetector-row computed tomography: scanning and contrast protocols*. Springer, New York, 2005.

[36] D. B. Plewes and P. B. Dean. The influence of partial volume averaging on sphere detectability in computed tomography. *Physics in Medicine and Biology*, 26(5):913–919, 1981.

[37] Brent S. Baxter A. Factors Affecting the Measurement of Size and CT Number in Computed Tomography. *Investigative Radiology*, (4):337–341, Nov-Dec 1981.

[38] E. L. Ritman. Molecular imaging in small animals - Roles for micro-CT. *Journal of Cellular Biochemistry*, 39:116–124, 2002.

[39] J. P. Gomilsek, I. Arcon, S. de Panfilis, and A. Kodre. X-ray absorption coefficient of iodine in the K-edge region. *Journal of Physics B-Atomic Molecular and Optical Physics*, 41(2).

[40] N. L. Ford, M. M. Thornton, and D. W. Holdsworth. Fundamental image quality limits for microcomputed tomography in small animals. *Medical Physics*, 30(11):2869–2877.

[41] Cristian T. Badea, Boma Fubara, Laurence W. Hedlund, and G. Allan Johnson. 4-D micro-CT of the mouse heart. *Mol Imaging*, 4(2):110–6, 2005.

[42] K. C. Graham, N. L. Ford, L. T. MacKenzie, C. O. Postenka, A. C. Groom, I. C. MacDonald, D. W. Holdsworth, M. Drangova, and A. F. Chambers. Non-invasive quantification of tumor volume in preclinical liver metastasis models using contrast-enhanced x-ray computed tomography. *Investigative Radiology*, 43(2):92–99, 2008.

[43] C. T. Badea, L. W. Hedlund, M. De Lin, J. F. B. Mackel, and G. A. Johnson. Tumor imaging in small animals with a combined micro-CT/micro-DSA system using iodinated conventional and blood pool contrast agents. *Contrast Media and Molecular Imaging*, 1(4):153–164, 2006.

[44] J. P. Weichert, F. T. Lee, M. A. Longino, S. G. Chosy, and R. E. Counsell. Lipid-based blood-pool CT imaging of the liver. *Academic Radiology*, 5:S16–S19, 1998.

[45] J. P. Weichert, F. T. Lee, S. G. Chosy, M. A. Longino, J. E. Kuhlman, D. M. Heisey, and G. E. Leverson. Combined hepatocyte-selective and blood-pool contrast agents for the CT detection of experimental liver tumors in rabbits. *Radiology*, 216(3):865–871, 2000.

[46] R. Fischbach, P. Landwehr, M. Svalund, H. G. Pape, H. G. Brochhagen, V. B. Kampenes, W. Heindel, and K. Lackner. Spiral CT angiography of the abdominal aorta - Comparison of iodixanol and ioversol. *Investigative Radiology*, 34(5):374–380, 1999.

[47] N. L. Ford, K. C. Graham, A. C. Groom, I. C. MacDonald, A. F. Chambers, and D. W. Holdsworth. Time-course characterization of the computed tomography contrast enhancement of an iodinated blood-pool contrast agent in mice using a volumetric flat-panel equipped computed tomography scanner. *Investigative Radiology*, 41(4):384–390, 2006.

[48] A. Chouker, M. Lizak, D. Schimel, T. HeImberger, J. M. Ward, D. Despres, I. Kaufmann, C. Bruns, F. Lohe, A. Ohta, M. V. Sitkovsky, B. Klaunberg, and

M. Thiel. Comparison of Fenestra VC contrast-enhanced computed tomography imaging with gadopentetate dimeglumine and Ferucarbotran magnetic resonance imaging for the in vivo evaluation of murine liver damage after ischemia and reperfusion. *Investigative Radiology*, 43(2):77–91, 2008.

[49] L. A. Feldkamp, L. C. Davis, and J. W. Kress. Practical cone-beam algorithm. *Journal of the Optical Society of America a-Optics Image Science and Vision*, 1(6):612–619, 1984.

[50] N. Otsu. A threshold selection method from gray-level histograms. *IEEE Transactions on Systems Man and Cybernetics*, 9(1):62–66, 1979.

[51] S. Phongkitkarun, S. Kobayashi, Z. X. Kan, T. Y. Lee, and C. Charnsangavej. Quantification of angiogenesis by functional computed tomography in a Matrigel model in rats. *Academic Radiology*, 11(5):573–582.

[52] R. M. Shaheen, D. W. Davis, W. B. Liu, B. K. Zebrowski, M. R. Wilson, C. D. Bucana, D. J. McConkey, G. McMahon, and L. M. Ellis. Antiangiogenic therapy targeting the tyrosine kinase receptor for vascular endothelial growth factor receptor inhibits the growth of colon cancer liver metastasis and induces tumor and endothelial cell apoptosis. *Cancer Research*, 59(21):5412–5416.

[53] T. M. Busch, S. M. Hahn, E. P. Wileyto, C. J. Koch, D. L. Fraker, P. Zhang, M. Putt, K. Gleason, D. B. Shin, M. J. Emanuele, K. Jenkins, E. Glatstein, and S. M. Evans. Hypoxia and photofrin uptake in the intraperitoneal carcinomatosis and sarcomatosis of photodynamic therapy patients. *Clinical Cancer Research*, 10(14):4630–4638, 2004.

[54] J. N. McGinley, K. K. Knott, and H. J. Thompson. Semi-automated method of quantifying vasculature of 1-methyl-1-nitrosourea-induced rat mammary carcinomas using immunohistochemical detection. *Journal of Histochemistry and Cytochemistry*, 50(2):213–222.

[55] Z. X. Kan, S. Phongkitkarun, S. Kobayashi, Y. Tang, L. M. Ellis, T. Y. Lee, and C. Charnsangavej. Functional CT for quantifying tumor perfusion in antiangiogenic therapy in a rat model. *Radiology*, 237(1):151–158.

[56] S. Hirakawa, S. Fujii, K. Kajiya, K. Yano, and M. Detmar. Vascular endothelial growth factor promotes sensitivity to ultraviolet B-induced cutaneous photodamage. *Blood*, 105(6):2392–2399, 2005.

[57] D. C. Yeh, D. V. Bula, J. W. Miller, E. S. Gragoudas, and J. G. Arroyo. Expression of leukocyte adhesion molecules in human subfoveal choroidal neovascular membranes treated with and without photodynamic therapy. *Investigative Ophthalmology and Visual Science*, 45(7):2368–2373.

[58] F. Kiessling, M. Krix, M. Heilmann, S. Vosseler, M. Lichy, C. Fink, N. Farhan, K. Kleinschmidt, L. Schad, N. E. Fusenig, and S. Delorme. Comparing dynamic parameters of tumor vascularization in nude mice revealed by magnetic resonance imaging and contrast-enhanced intermittent power Doppler sonography. *Investigative Radiology*, 38(8):516–524, 2003.

[59] N. Ojha, S. Roy, G. He, S. Biswas, M. Velayutham, S. Khanna, P. Kuppusamy, J. L. Zweier, and C. K. Sen. Assessment of wound-site redox environment and the significance of Rac2 in cutaneous healing. *Free Radical Biology and Medicine*, 44(4):682–691.

[60] P. R. Twentyman, J. M. Brown, J. W. Gray, A. J. Franko, M. A. Scoles, and R. F. Kallman. A new mouse tumor model system (RIF-1) for comparison of end-point studies. *Journal of the National Cancer Institute*, 64(3):595–604.

[61] E. L. Ritman. Small-animal CT: Its difference from, and impact on, clinical CT. *Nuclear Instruments and Methods in Physics Research Section A - Accelerators Spectrometers Detectors and Associated Equipment*, 580(2):968–970, 2007.

[62] A. Mariampillai, B. A. Standish, E. H. Moriyama, M. Khurana, N. R. Munce, M. K. K. Leung, J. Jiang, A. Cable, B. C. Wilson, I. A. Vitkin, and V. X. D. Yang. Speckle variance detection of microvasculature using swept-source optical coherence tomography. *Optics Letters*, 33(13):1530–1532, 2008.

[63] V. H. Fingar, P. K. Kik, P. S. Haydon, P. B. Cerrito, M. Tseng, E. Abang, and T. J. Wieman. Analysis of acute vascular damage after photodynamic therapy using benzoporphyrin derivative (BPD). *British Journal of Cancer*, 79(11-12):1702–1708, 1999.

[64] Raymond F. Muzic Jr. Chris Flask David L. Wilson Jeffrey L. Duerk Denise K. Feyes Baowei Fei, Hesheng Wang and Nancy L. Oleinick. Deformable and rigid registration of MRI and microPET images for photodynamic therapy of cancer in mice. *Med. Phys.*, 33(3):756–760, 2003.

[65] G. Q. Yu, T. Durduran, C. Zhou, H. W. Wang, M. E. Putt, H. M. Saunders, C. M. Sehgal, E. Glatstein, A. G. Yodh, and T. M. Busch. Noninvasive monitoring of murine tumor blood flow during and after photodynamic therapy provides early assessment of therapeutic efficacy. *Clinical Cancer Research*, 11(9):3543–3552, 2005.

[66] K. Kurobane, A. Tominaga, K. Sato, J. R. North, Y. Namba, and N. Oku. Photodynamic therapy targeted to tumor-induced angiogenic vessels. *Cancer Letters*, 167(1):49–56, 2001.

[67] B. Chen, T. Roskams, Y. Xu, P. Agostinis, and P. A. M. de Witte. Photodynamic therapy with hypericin induces vascular damage and apoptosis in the RIF-1 mouse tumor model. *International Journal of Cancer*, 98(2):284–290, 2002.

[68] I. P. J. vanGeel, H. Oppelaar, Pfjw Rijken, Hjja Bernsen, N. E. M. Hagemeier, A. J. vanderKogel, R. J. Hodgkiss, and F. A. Stewart. Vascular perfusion and

hypoxic areas in RIF-1 tumours after photodynamic therapy. *British Journal of Cancer*, 73(3):288–293, 1996.

[69] B. Chen, B. W. Pogue, J. M. Luna, R. L. Hardman, P. J. Hoopes, and T. Hasan. Tumor vascular permeabilization by vascular-targeting photosensitization: Effects, mechanism, and therapeutic implications. *Clinical Cancer Research*, 12(3):917–923, 2006.

[70] S. P. Robinson, P. Rijken, F. A. Howe, P. M. J. McSheehy, B. P. J. van der Sanden, A. Heerschap, M. Stubbs, A. J. van der Kogel, and J. R. Griffiths. Tumor vascular architecture and function evaluated by non-invasive susceptibility MRI methods and immunohistochemistry. *Journal of Magnetic Resonance Imaging*, 17(4):445–454.

[71] T. C. Zhu and J. C. Finlay. The role of photodynamic therapy (PDT) physics. *Medical Physics*, 35(7):3127–3136, 2008.

[72] W. Ross, D. D. Cody, and J. D. Hazle. Design and performance characteristics of a digital flat-panel computed tomography system. *Medical Physics*, 33(6):1888–1901, 2006.

[73] F. Kiessling, S. Greschus, M. P. Lichy, M. Bock, C. Fink, S. Vosseler, J. Moll, M. M. Mueller, N. E. Fusenig, H. Traupe, and W. Semmler. Volumetric computed tomography (VCT): a new technology for noninvasive, high-resolution monitoring of tumor angiogenesis. *Nature Medicine*, 10(10):1133–1138, 2004.

[74] Steven M. Jorgensen, Omer Demirkaya, and Erik L. Ritman. Three-dimensional imaging of vasculature and parenchyma in intact rodent organs with X-ray micro-CT. *American Journal of Physiology*, 275(3 PART 2):H1103–H1114, 1998.

[75] L. Y. Du, J. Umoh, H. N. Nikolov, S. I. Pollmann, T. Y. Lee, and D. W. Holdsworth. A quality assurance phantom for the performance evaluation of

volumetric micro-CT systems. *Physics in Medicine and Biology*, 52(23):7087–7108, 2007.

[76] R. Gupta, M. Grasruck, C. Suess, S. H. Bartling, B. Schmidt, K. Stierstorfer, S. Popescu, T. Brady, and T. Flohr. Ultra-high resolution flat-panel volume CT: fundamental principles, design architecture, and system characterization. *European Radiology*, 16(6):1191–1205, 2006.